Volume 1 | Number 1 | Jan 2013 | Pages 1–100

PCCP

Physical Chemistry Chemical Physics
www.rsc.org/pccp

ROYAL SOCIETY OF CHEMISTRY

ROYAL SOCIETY OF CHEMISTRY

www.rsc.org/pccp

Journal Name

Physical Chemistry Chemical Physics

ARTICLE TYPE

Simultaneous Detection of Electronic Structure Changes from Two Elements of a Bifunctional Catalyst Using Wavelength-Dispersive X-ray Emission Spectroscopy and *in situ* Electrochemistry

Sheraz Gul[a,f], Jia Wei Desmond Ng[b], Roberto Alonso-Mori[c], Jan Kern[a,c], Dimosthenis Sokaras[c], Eitan
5 **Anzenberg[d], Benedikt Lassalle-Kaiser[a,#], Yelena Gorlin[b,%], Tsu-Chien Weng[c], Petrus H. Zwart[e], Jin Z.**
Zhang[f], Uwe Bergmann[c], Vittal K. Yachandra[a], Thomas F. Jaramillo[b,d,*] and Junko Yano[a,d,*]

Multielectron catalytic reactions, such as water oxidation, nitrogen reduction, or hydrogen production in
10 enzymes and inorganic catalysts often involve multimetallic clusters. In these systems, the reaction takes place between metals or metals and ligands to facilitate charge transfer, bond formation/breaking, substrate binding, and release of products. In this study, we present a method to detect X-ray emission signals from multiple elements simultaneously, which allows for the study of charge transfer and the sequential chemistry occurring between elements. Kβ X-ray emission spectroscopy (XES) probes charge
15 and spin states of metals as well as their ligand environment. A wavelength-dispersive spectrometer based on the von Hamos geometry was used to disperse Kβ signals of multiple elements onto a position detector, enabling an XES spectrum to be measured in a single-shot mode. This overcomes the scanning needs of the scanning spectrometers, providing data free from temporal and normalization errors and therefore ideal to follow sequential chemistry at multiple sites. We have applied this method to study
20 MnO$_x$-based bifunctional electrocatalysts for the oxygen evolution reaction (OER) and the oxygen reduction reaction (ORR). In particular, we investigated the effects of adding a secondary element, Ni, to form MnNiO$_x$ and its impact on the chemical states and catalytic activity, by tracking the redox characteristics of each element upon sweeping the electrode potential. The detection scheme we describe here is general and can be applied to time-resolved studies of materials consisting of multiple elements, to
25 follow the dynamics of catalytic and electron transfer reactions.

Introduction

Many of the catalytic reactions in inorganic systems and enzymes involve multiple electrons, and go through several intermediate steps. In natural systems, the rate and the directionality of the
30 electron-flow are well-controlled during the reaction, by spatially and temporally separated moieties within molecules, or between pigments, or between one system and another. Similarly, controlling the electron flow between multiple sites in inorganic systems is a key issue for developing materials such as artificial
35 photosynthetic devices and magnetic materials. In this work, we present an X-ray emission spectroscopy (XES) detection scheme to simultaneously follow the chemistry at multiple sites by probing the element/orbital/spin-specific signals, leading to a better understanding of the dynamics of catalysis and electron
40 transfer reactions.

XES has proved to be a powerful technique in the past few years with the development of high brilliance X-ray beamlines at modern synchrotron radiation sources. Complementary to X-ray absorption spectroscopy (XAS), XES probes occupied electronic

45 orbitals of elements by measuring photons emitted from orbitals at higher energy into a 1s hole (K-emission) after the excitation event. Each emission line is characteristic of the orbital that the electron is emitted from, and contains unique chemical information such as charge/spin state, ligand properties, and
50 symmetry.[1] Among the various X-ray emission lines, Kβ$_{1,3}$ and Kβ' transitions correspond to metal 3p to 1s decays, and their peak positions reflect the number of unpaired electrons through the 3p/3d exchange interaction. Therefore, the spectra are sensitive to the oxidation state and spin state of the metal site.
55 XES has been used recently to provide local geometric/electronic structures of an element of interest in the field of metalloenzymes and inorganic catalysts.[2-6]

Unlike other X-ray spectroscopy techniques, XES is capable of simultaneously probing multiple metal sites in the sample. As
60 shown in **Scheme 1**, single incident X-ray energy can excite metals when it is above their electron binding energy without the requirement monochromatic incoming X-rays. The use of a wavelength-dispersive spectrometer combined with a position sensitive detector (PSD) further eliminates the need to scan the
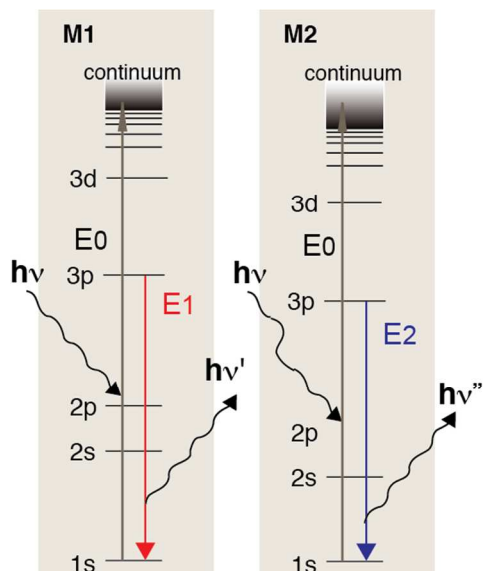
Scheme 1: Kβ energy diagram showing two elements being excited simultaneously with the same incoming X-ray beam (E_0).

Fig. 1 (a) A representative SEM image of $MnNiO_x$ sample deposited on Au-Si_3N_4. **(b)** Cyclic voltammograms of electrodeposited $MnNiO_x$ (blue), MnO_x (red), NiO_x (green), and blank Au-Si_3N_4 (black) in 0.1 M KOH. Data was collected at a sweep rate of 20 mV·s^{-1}.

photon-out spectrum (i.e. to scan crystals analyzer and detector positions), unlike commonly used spectrometers based on scanning geometries. Recently, we have developed a multi-crystal von Hamos type spectrometer designed for shot-by-shot collection of emission spectra.[7] The spectrometer has been used to take shot-by-shot measurements at an X-ray free electron laser facility, enabling the use of XES simultaneously with other techniques such as X-ray Diffraction (XRD) and other scattering measurements.[8-11] In the current study, we used the wavelength-dispersive spectrometer to probe multiple metal sites simultaneously by different crystal reflections that disperse the emission signal from each metal into a separate line on the PSD detector. Although spectrometers that work in scanning mode provide better signal to background ratios owing to their one-to-one focusing geometry, the advantages of measuring multiple elements simultaneously using wavelength-dispersive spectrometers exceed when the main focus is to understand sequential changes that occur among multiple elements. The detection scheme proposed here simplifies the comparison of the changes in different element sites by circumventing systematic errors often induced by the concentration and volume distribution of the sample, data normalization, and timing errors when measurements are conducted independently.

In the present study, we have investigated the MnO_x-based bifunctional electrocatalyst, and more specifically the effects of adding a secondary element, Ni. Using this new detection scheme, we have followed the simultaneous changes in the electronic structure of Mn and Ni by XES as a function of the applied electrochemical potential. The MnO_x-based catalyst can catalyze both the oxygen reduction reaction (ORR) and the oxygen evolution reaction (OER). The development of catalytic materials that can effectively catalyze interconversion between O_2 and H_2O is important to enable renewable energy technologies, including fuel cells, metal-air batteries, electrolysis cells, and solar fuel synthesis. For example, OER catalysts play a key role in artificial photosynthesis while the ORR is the cathode reaction in fuel cells. Regenerative fuel cells and metal air batteries
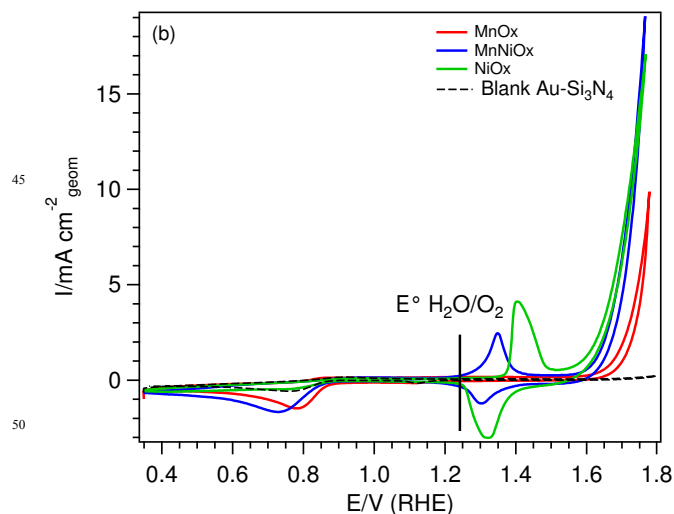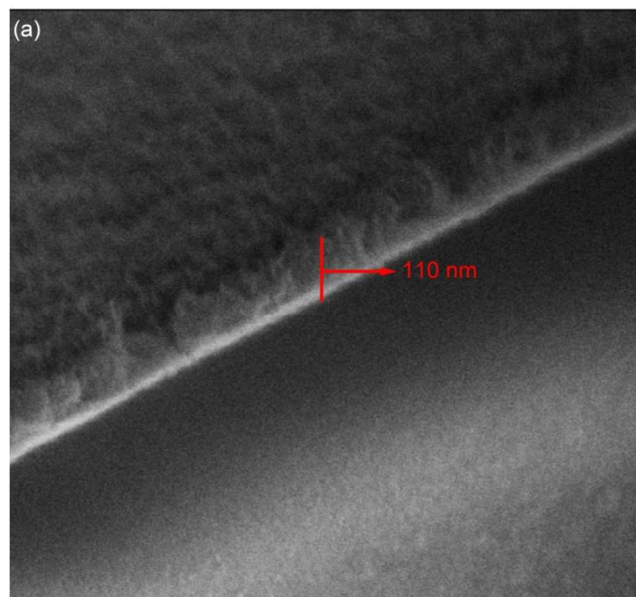
require oxygen catalysts that are effective at both the OER and the ORR. In order to develop improved catalysts, it is necessary to understand the chemical state of catalysts under reaction conditions.

Often, multi-metallic systems exhibit improved activity compared to a single metal-based system within oxide-based electrocatalysts for OER and/or ORR catalysis.[12] In the current study, we employed XES to investigate the effect of adding Ni into a MnO_x-based OER and ORR bifunctional electrocatalyst. The presence of Ni in MnO_x has been reported to modify the reaction kinetics and electrochemical stability of the catalyst.[13, 14] The XES detection scheme we introduce here is suitable for investigating the chemistry that occurs at the two metal sites. In addition, *in situ* XES results have been complimented by *in situ* XAS measurements, providing structural aspects of the catalysts.
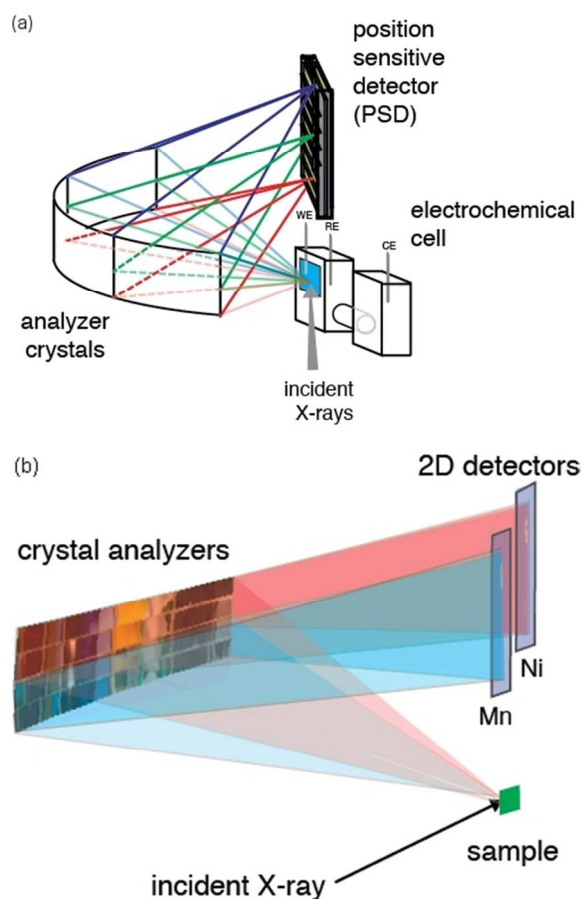
Fig. 2 (a) Experimental setup for wavelength-dispersive XES with an *in situ* electrochemical cell; WE, RE and CE denote working electrode, reference electrode and counter electrode, respectively. **(b)** Schematic representation of the setup for simultaneous detection of XES from two elements with the von Hamos spectrometer. The pink and blue traces correspond to the two scattering pathways for photons emitted by two different elements.

Results

MnNiO$_x$ Catalyst

A representative SEM image of the electrodeposited MnNiO$_x$ film on Au-Si$_3$N$_4$ is shown in **Fig. 1a**, with an estimated sample thickness of 110 nm. The cyclic voltammograms of MnNiO$_x$, MnO$_x$, NiO$_x$, and blank Au-Si$_3$N$_4$ substrate are shown in **Fig. 1b**. Clearly, all three catalysts are active for the OER as they outperform the bare Au-Si$_3$N$_4$ substrate, with the MnNiO$_x$ and NiO$_x$ displaying higher activity than pure MnO$_x$. For the ORR, direct comparisons are more challenging as there are mass transport limitations given the cell conditions and the fact that the Au in the Au-Si$_3$N$_4$ substrate itself exhibits considerable ORR activity; Au is a known ORR catalyst in basic media.[15] The NiO$_x$ system exhibits comparable ORR activity to that of the bare substrate, thus it is unclear whether the NiO$_x$ is active or if the Au substrate is catalyzing the reaction. However, both the MnNiO$_x$ and the MnO$_x$ samples display higher activity than the substrate for the ORR, with the MnO$_x$ exhibiting a slightly earlier onset potential than MnNiO$_x$, reflecting higher activity.

The cyclic voltammogram of the MnO$_x$ catalyst displays no observable redox peaks which is consistent with previous studies
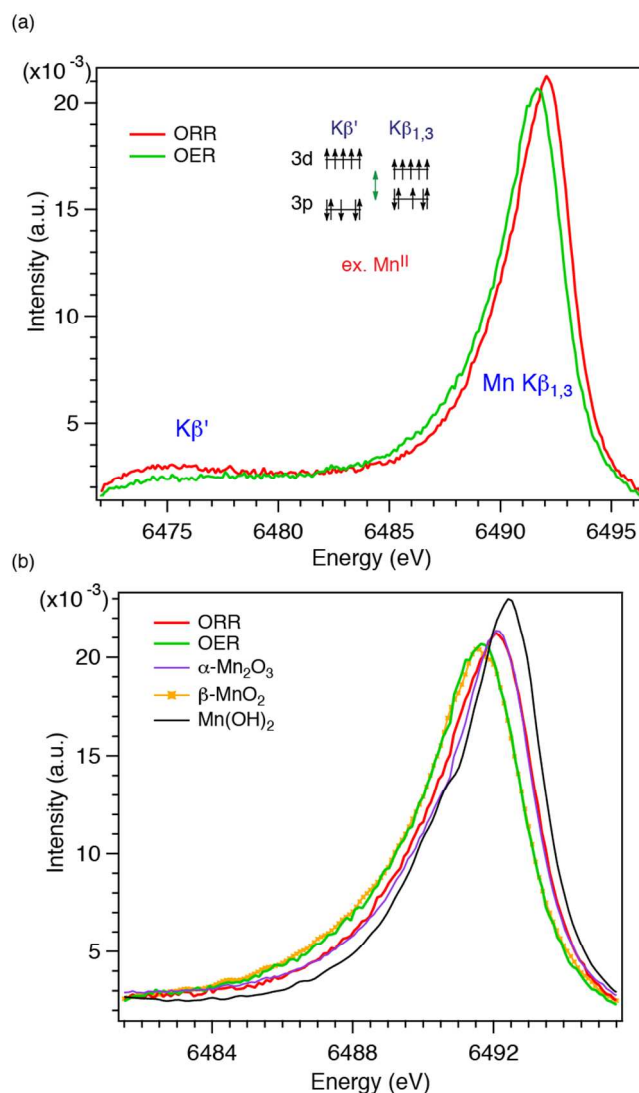

Fig. 3 (a) Mn Kβ$_{1,3}$ XES spectra of the MnNiO$_x$ catalyst at 0.6 V (ORR) and 1.8 V (OER). The inset shows the transition scheme of the Kβ$_{1,3}$ and Kβ′ emission process for Mn^{II}. **(b)** Comparison of the XES spectra of Mn oxide standards to the ORR phase and the OER phase of the MnNiO$_x$ catalyst. The spectra are normalized by area in the energy range 6482-6496 eV.

on a number of MnO$_x$ catalysts.[16, 17] For the NiO$_x$ catalyst, only one redox feature is observed at 1.35-1.45 V, which corresponds to the Ni^{II}/Ni^{III} to Ni$^{III/IV}$ oxidation as shown from the XAS and XES results described below. We found that for the MnNiO$_x$ catalyst, the same redox couple was shifted to lower potentials compared to that of NiO$_x$, which suggests that Mn and Ni are mixed into the lattice at electrochemically active sites and that the presence of the two metals can affect one another's redox potential.

In situ **Wavelength-Dispersive XES Data Collection for Studying Multiple Element Systems**

We have used wavelength-dispersive XES to study electronic structural changes of the MnNiO$_x$ catalyst. The XES setup is shown in **Fig. 2**. The spectrometer provides high energy resolution (~0.6 eV) and a large solid angle of collection (1.3 % of the sphere). An array of up to 4x4 crystal analyzers diffracts and focuses the emitted radiation from the sample onto a PSD

detector following Bragg's law, $n\lambda = 2d\sin\theta$. The crystal analyzers, which are 110 x 25 mm^2 (horizontal x vertical), are cylindrically bent with a curvature radius of 500 mm perpendicular to the scattering plane. For each crystal analyzer, integration along the focusing direction of the signal on the detector results in an emission spectrum. This setup enables an XES spectrum to be measured in a wavelength-dispersive mode, overcoming the scanning needs of the Rowland circle spectrometers.[7] The angle between the incident and emitted X-rays (scattering angle) was set to 90 degrees to minimize the background contribution of the elastic scattering from the sample.

A subset of 12 Si(440) crystals was used to collect the signal from the Mn Kβ region 6472 eV to 6498 eV, corresponding to a Bragg angle from 86.1 to 83.6 degrees and focus it to one line on a Pilatus 100k detector. A second Pilatus 100k detector was used to record the Ni Kβ signal (8235 eV to 8300 eV) from a second subset of 4 Si(551) crystals covering a Bragg angle from 81.8 to 79.2 degrees.

In Situ XES under ORR and OER conditions

Using wavelength-dispersive XES, we collected the Kβ$_{1,3}$ and Kβ' XES spectra of Mn and Ni from the MnNiO$_x$ bifunctional electrocatalyst under electrochemical reaction conditions.

Fig. 3a shows the Mn Kβ$_{1,3}$ and Kβ' emission spectra for the MnNiO$_x$ bifunctional electrocatalyst under ORR and OER conditions collected at 0.6 V and 1.8 V. The Kβ$_{1,3}$ peak arises from the emission process of the Mn $3p$ to $1s$ transition, with constructive spin configuration. The accompanying Kβ' peak corresponds to the destructive spin configuration; the mechanism has been illustrated by a schematic representation in the inset of Fig. 3a. Together, both peaks reflect the number of unpaired electrons through the $3p/3d$ spin exchange interactions. There is a smaller $3p/3d$ exchange interaction with the decrease in spin and the Kβ$_{1,3}$ and Kβ' peaks move towards each other with decreasing spin. Kβ lines are thus sensitive to the spin state of a metal. More precisely, they reflect the effective number of unpaired metal $3d$ electrons, which takes into account the covalency of the metal ligand bond.

Upon changing the potential from 0.6 V to 1.8 V, a shift in the Mn Kβ$_{1,3}$ peak position to lower energies is observed in Fig. 3a, indicating a change to higher oxidation state of Mn as the energy gap between $3p$ and $1s$ levels decreases. This is accompanied by the intensity changes in the Kβ' region; a decreased peak intensity is due to the low probability of the $3p/3d$ spin exchange interaction in Mn with higher oxidation states, and consistent with the oxidation state changes. **Fig. 3b** compares the Mn XES spectra of the ORR phase (0.6 V) and the OER phase (1.8 V) with those of Mn oxides with different oxidation states. The area under the curves was normalized to 1 in the energy range 6482-6496 eV. The Kβ$_{1,3}$ Mn spectrum for ORR catalyst lies close to that of α-Mn$_2$O$_3$ towards the high energy side, indicating the existence of Mn^{3+}. A slight difference between these spectra on the low energy side, however, suggests the presence of a fraction of Mn^{4+} in the ORR phase, as the Kβ$_{1,3}$ peak extends further towards lower energies as compared to α-Mn$_2$O$_3$. Therefore, the oxidation state of Mn lies between +3 and +4 under ORR conditions. When the potential is changed to 1.8 V, corresponding to the OER phase, the Kβ$_{1,3}$ spectrum obtained overlays well with that of β-MnO$_2$ as shown in Fig. 3b. This

(a)

(b)

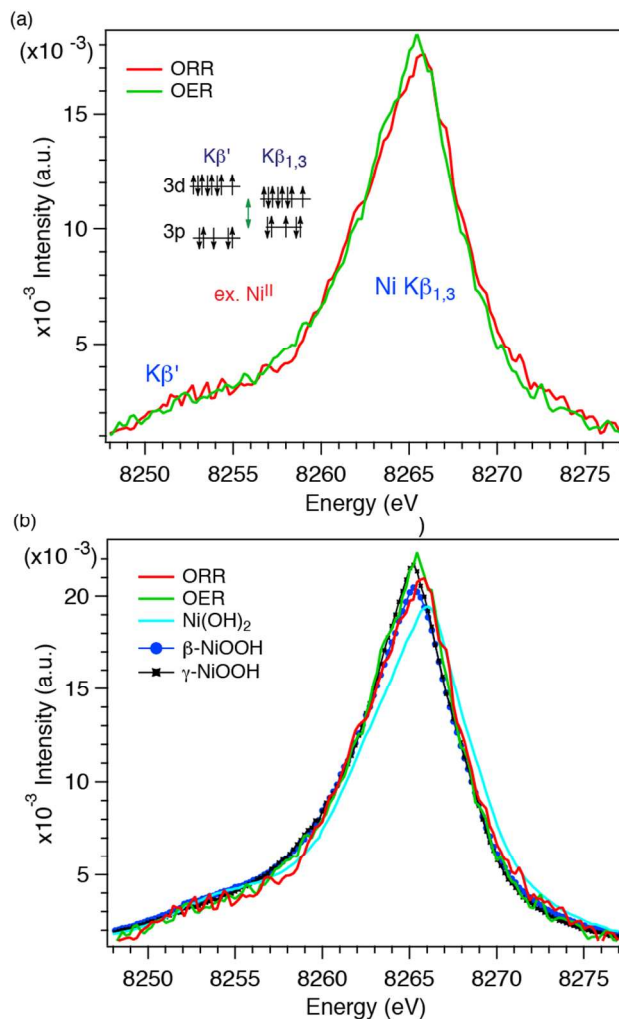**Fig. 4 (a)** Kβ$_{1,3}$ XES spectra of Ni at 0.6 V (ORR) and 1.8 V (OER). The inset shows the transition scheme of the Kβ$_{1,3}$ and Kβ' emission process for Ni^{II}. Svitzky-Golay smoothing procedure was employed using a second order polynomial and 5 data points for each smoothed output value computed. **(b)** Comparison of the XES spectra of Ni oxide standards to the ORR and OER Phases.

suggests an overall oxidation state of +4 for Mn under OER conditions.

The Ni spectra of ORR and OER phases of the MnNiO$_x$ bifunctional electrocatalyst are shown in **Fig. 4a**. The spectra have been smoothed with the Svitzky-Golay algorithm using a second order polynomial and 5 data points for each smoothed output value. The area under the spectra between 8248.0-8276.0 eV was normalized to 1. The peak shifts in the Ni spectra between the ORR and OER potentials are not as clear as those observed in the Mn XES. Overall, however, the Kβ$_{1,3}$ peak in the ORR phase is at slightly higher energy than that in the OER phase. In **Fig. 4b**, the spectra under ORR and OER conditions are plotted together with those of Ni oxides with different oxidation states. The Kβ$_{1,3}$ peak for the ORR phase is at lower energy as compared to that of Ni(OH)$_2$, but at higher energy than β-NiOOH which has Ni in +3 oxidation state. This indicates that the oxidation state of Ni during the ORR is between +2 and +3. On the other hand, the peak position and spectral shape of the OER phase closely resemble those of γ-NiOOH. The oxidation state of
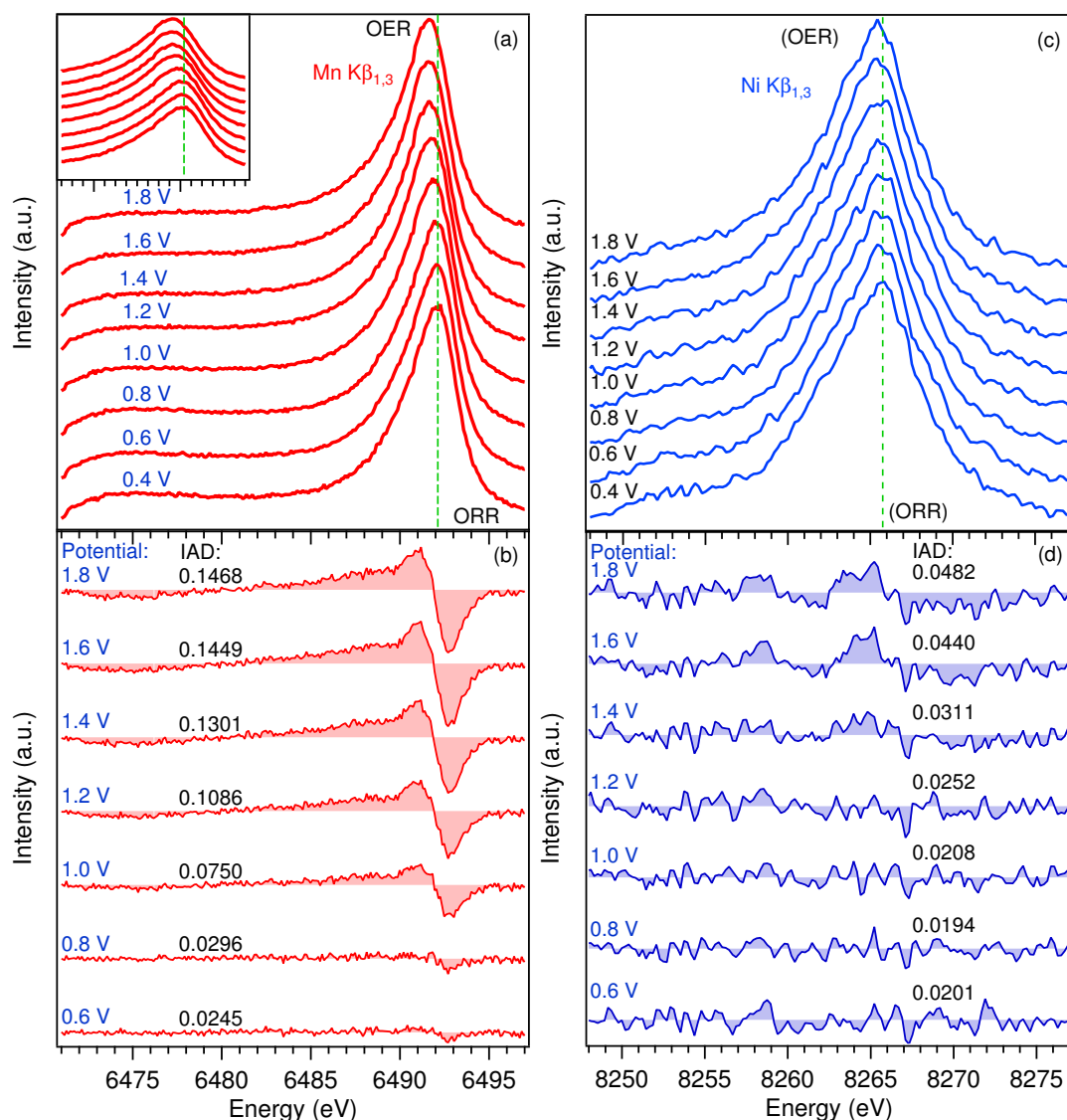
Fig. 5 (a) Evolution of the Mn $K\beta_{1,3}$/$K\beta'$ XES spectra of MnNiO$_x$ electrocatalyst measured at the potentials indicated while step wise sweeping of the potential. No smoothing was done for Mn spectra. The inset shows a zoomed-in view of the main peak to highlight the changes in its position. **(b)** Difference spectra at the indicated potentials obtained by using the spectrum at 0.4 V as a reference spectrum. **(c)** Evolution of the Ni $K\beta_{1,3}$/$K\beta'$ XES spectra of MnNiO$_x$ electrocatalyst measured at the potentials indicated while step wise sweeping of the potential. The spectra were smoothed with the Svitzky-Golay algorithm using a second order polynomial and 5 data points for each smoothed output value. **(d)** Difference spectra at the indicated potentials obtained by using the spectrum at 0.4 V as a reference spectrum. Absolute values of integrated difference (IAD) using 0.4 V spectrum as the reference are also shown in (b) and (d). IAD values were calculated for the energy range of 6471.0-6497.0 eV for Mn and 8248.0-8276.0 eV for Ni.

Ni in γ-NiOOH is approximately +3.7.[18-20] This suggests that the oxidation state of Ni in the MnNiO$_x$ film is between +3 and +4 under OER conditions and very close to that of Ni in γ-NiOOH. It is worth noting that the $K\beta_{1,3}$ peak shift is much smaller in Ni as compared to Mn among the different oxidation states. This arises from the differences in their electronic configuration, as shown in the insets of Fig. 3a and Fig. 4a, and covalency of metal-ligand bonds. Additionally, the $K\beta_{1,3}$ and $K\beta'$ peaks are close to each other due to the limited number of unpaired spins in Ni 3d orbitals. This is observed experimentally by a smaller intensity for Ni(OH)$_2$ (Ni^{II} has two unpaired electrons in O$_h$, high spin configuration) than for β- and γ-NiOOH (Ni^{III} and Ni^{IV} have three and four unpaired electrons in O$_h$, high spin configuration).

Phase Evolution between the ORR and the OER

To investigate the transitions between the ORR and OER phases during stepped electrochemical cycling, *in-situ* $K\beta$ XES of Mn and Ni were measured while stepwise sweeping of the potential(in 0.2 V steps) along the CV curve between 0.4 V to 1.8 V vs RHE. **Fig. 5a** shows a series of Mn $K\beta$ XES spectra of the MnNiO$_x$ catalyst. The collection time for each spectrum was 60 minutes during which the corresponding potential was held constant. With the change in potential, a gradual change in the energy of the $K\beta_{1,3}$ peak maximum was observed; the peak progressively shifts to lower energies with increasing applied potentials. This shift can be seen more clearly in the inset of Fig.
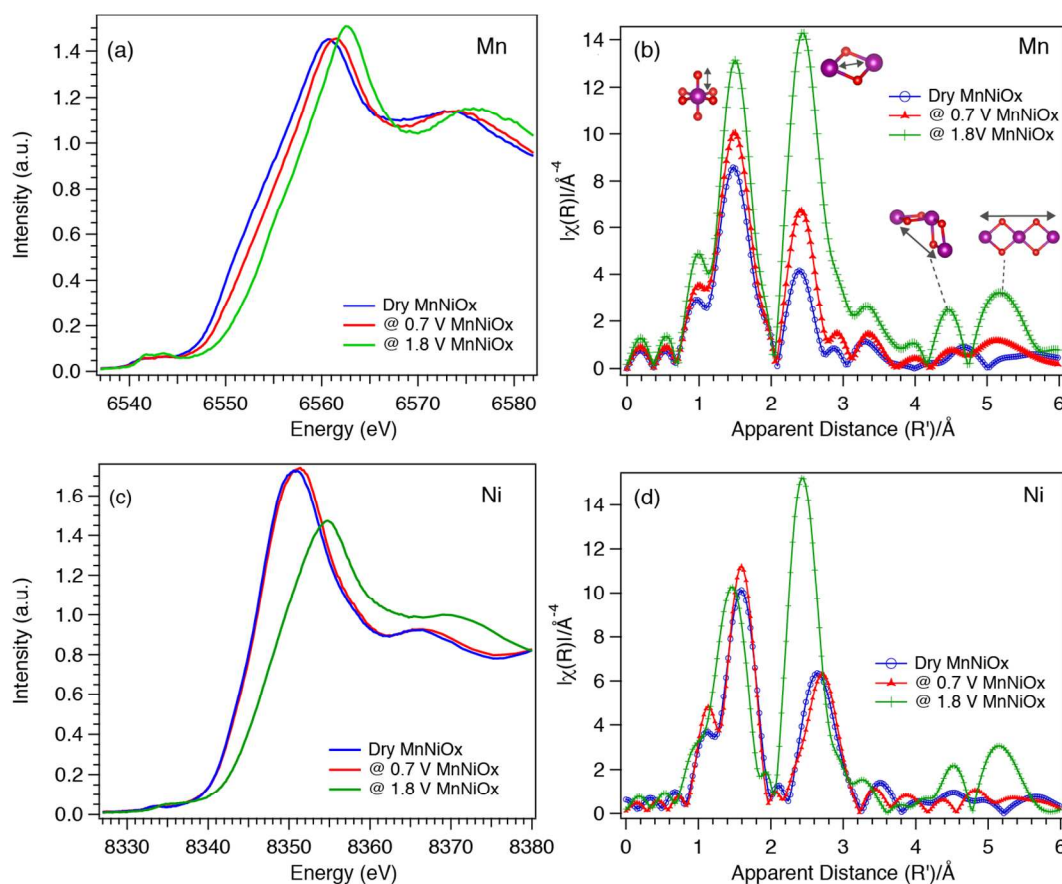
ARTICLE TYPE

Fig. 6 Mn and Ni *K*-edge XAS spectra of MnNiO$_x$ under ORR (0.7 V) and OER (1.8 V) conditions. **(a)** Mn XANES, **(b)** Mn EXAFS, metal atoms are shown as purple spheres and O atoms as red spheres **(c)** Ni XANES and **(d)** Ni EXAFS spectra of MnNiO$_x$.

5a.

The K$\beta_{1,3}$ peak is normally asymmetric due to the final states involving spin-flip excitations accompanying the 3*p* to 1*s* decay. This is a many-electron-effect as upon transition of a 3*p* electron to 1*s*, another electron in 3*d* reacts to the change in electron configuration by flipping its spin. This configuration is responsible for the broad tail on the low energy side of the main peak.[21, 22] For such an asymmetric peak, comparing the integrated absolute difference (IAD) is a more sensitive approach as compared to the 1st moment analysis as shown by Vankó *et al.*[23, 24] This analysis is based on the absolute value of the difference between a reference spectrum and a sample spectrum.

$$IAD_i = \int \left| \sigma_i^{XES}(E) - \sigma_0^{XES}(E) \right| dE$$

where XES spectrum σ_0 is the reference spectrum and σ_i is the XES spectrum for which the IAD value is to be calculated. We used the XES spectrum collected at 0.4 V as the reference spectrum (σ_0), and difference spectra were obtained by subtracting the reference spectrum from spectra measured at different potentials. Before the subtraction, all the spectra were area normalized in the energy range of 6471.0-6497.0 eV. The difference spectra are shown in **Fig. 5b** along with the calculated IAD values. The negative peak on the high energy side (6493 eV) along with the accompanying positive peak (6491 eV) arise from a shift in the main peak to lower energy with increasing potential. However, the broad positive feature on the low energy side of the positive peak (~ 6491.0 eV) stems from the increased intensity of the K$\beta_{1,3}$ low energy shoulder, and broadening of the K$\beta_{1,3}$ peak at higher potentials. The negative peak around 6475 eV originates from the decrease in intensity of the Kβ' peak at higher potential when Mn becomes more oxidized. This is also a good measure of the decrease in effective number of unpaired electrons on Mn in MnNiO$_x$ as the potential increases.

The Ni K$\beta_{1,3}$ spectra, collected simultaneously with those of Mn, are shown in **Fig. 5c**. Spectra were smoothed by employing the Svitzky-Golay algorithm where a second order polynomial and 5 data points were used to compute each smoothed output value. The area under the spectra between 8248.0-8277.0 eV was normalized to 1. To get a more quantitative view of the change,

IAD analysis was carried out using the 0.4 V spectrum as the reference. The corresponding difference spectra are plotted in **Fig. 5d** along with the associated IAD values. The change is small but noticeable, in particular, in the last three spectra collected at 1.4, 1.6, and 1.8 V as indicated by the corresponding IAD values. These spectra are mainly composed of two pairs of peaks with opposite signs between 8255.0-8276.0 eV. The differences arise from the shift of the main peak towards lower energy along with slight narrowing of the peak, which indicates an increase in the oxidation state.

In Situ XAS

Structural information for the catalysts was obtained by Mn and Ni XAS. *In situ* XAS spectra were measured while exposing the sample to ORR and OER relevant potentials of 0.7 V and 1.8 V, respectively. For XAS studies, 0.7 V was chosen as the potential corresponding to the ORR phase, as *in situ* XAS measurements in our previous study have been reported under this potential;[25] no significant changes are observed up to 0.8 V (Fig. 5). Both Ni and Mn *K*-edge XANES and EXAFS spectra corresponding to the ORR and OER phase are shown in **Fig. 6**.

Mn XANES and EXAFS

Fig. 6a compares the Mn *K*-edge XANES of the ORR and OER phases along with the dry (as-prepared) catalyst. Increasing the potential from ORR to OER conditions results in oxidation of Mn as indicated by the shift of the edge position to higher energy. In **Fig. S1** of the electronic supplemental information (ESI), XANES spectra of the ORR and OER phases are compared with the spectra of Mn oxides. Based on the edge position, the ORR phase (6552.2 eV at the half-height of the absorption edge) is more oxidized than $Mn_3^{II,III,III}O_4$ (6548.5 eV) and $\alpha-Mn_2^{III}O_3$ (6550.9 eV), and closely resembles birnessite (6552.3 eV) phase (Fig. S1a). Birnessite, which is a naturally occurring Mn mineral, has a layered structure with intercalating cations (M^{n+}) and water molecules between the layers. Synthetic forms of birnessite like triclinic Mg^{2+}-birnessite, normally have 20-40% Mn^{III} in $Mn^{IV}O_2$,[26-28] leading to an average oxidation state of 3.6-3.8. The XANES data recorded on the $MnNiO_x$ film under ORR conditions therefore confirms an oxidation state of Mn higher than +3, as found from XES measurements.

The rising edge position (6553.8 eV) of the catalyst held at an OER relevant potential appears at higher energy than those of $\alpha-Mn_2^{III}O_3$, birnessite and todorokite (6553.0 eV), indicating that the catalytic phase is more oxidized than these reference samples (ESI Fig. S1b). The edge position of the OER phase is very close to those of $\beta-MnO_2$ (6553.5 eV) and $\lambda-MnO_2$ (6553.2 eV). This shows that the Mn^{IV} content of the OER phase is higher than that in birnessite or todorokite, suggesting an oxidation state of ~ +4.0 for the catalyst held at an OER relevant potential, confirming the XES results.

Fourier transform of k^3-weighted EXAFS are shown in Fig. 6 (b) for the dry, ORR and OER phases. Note that the distances indicated by the peak positions are shorter by ~0.5 Å relative to the true distances, due to the phase shift. The structural motifs corresponding to each peak are shown with arrows highlighting the absorber scatterer pairs. The EXAFS Fourier transform (FT) spectrum of the ORR phase is compared with the reference spectra of MnOOH, birnessite and todorokite in **Fig. S2a** in the ESI, and shows strong similarities with birnessite, thus

confirming the XANES observation. The first and second neighbor distances obtained from EXAFS curve fitting are reported in ESI **Table S1**, and comparable values were obtained for the birnessite and the ORR phase. The ORR spectrum also shows similarities with the todorokite phase, which can accommodate other cations in the structure. However, the birnessite-like phase is more likely as this phase can be formed electrochemically at room temperature,[29, 30] whereas formation of the todorokite-like phase generally requires high temperature or pressure.[28, 31] Thus, under ORR conditions the catalytic phase has Mn in an oxidation state close to that of birnessite. For the OER phase, some resemblance to the EXAFS spectra of $\lambda-MnO_2$ was observed, consistent with the XANES observation.

Ni XANES and EXAFS

Ni *K*-edge XANES spectra of $MnNiO_x$ corresponding to dry, ORR and OER conditions are shown in Fig. 6c. In switching from ORR to OER relevant potentials, the Ni edge position shifts by +2.4 eV, from 8343.4 to 8345.8 eV (measured by the half edge jump position). The XANES spectrum of the ORR phase was compared with the Ni oxide standards, $Ni(OH)_2$, $NaNiO_2$, $\beta-NiOOH$, and $\gamma-NiOOH$, and nickel potassium paraperiodate (NiPPI) with formal oxidation states of +2, +3, +3, +3.7 and +4, respectively (see SI **Fig. S3a**). The half-edge position of the ORR phase (8343.4 eV) appears at ~1.0 eV higher energy than $Ni(OH)_2$ (8342.7 eV) and is very close to $\beta-NiOOH$ (8343.9 eV) and $NaNiO_2$. The white line energy of the ORR phase lies between those of $Ni(OH)_2$ and $\beta-NiOOH$. The result indicates that the Ni oxidation state of the ORR phase is between +2 and +3, corroborating the XES results. The XANES spectrum of the OER phase shows a strong resemblance to $\gamma-NiOOH$ (see the ESI, **Fig. S3b**, with an oxidation state of +3.7.[18-20, 32]

Fig. 6d shows the Ni FT EXAFS spectra of the dry sample along with those under catalytic conditions, whereas EXAFS spectra of the ORR and OER phases were compared with those of model compounds, including $Ni(OH)_2$, $NaNiO_2$, $\beta-NiOOH$, $\gamma-NiOOH$, and NiPPI in ESI **Fig. S4**. As observed in XANES, the ORR spectrum does not match with any of the reference compounds. The second peak corresponding to the second neighbor shell is observed at a slightly shorter distance (~ 3.06 Å) as compared to $Ni(OH)_2$ (~ 3.12 Å) (see ESI Table S1). Contrary to the ORR phase, considerable similarities are noticed between the spectra of the OER phase and $\gamma-NiOOH$ (ESI **Fig. S4b** and Table S1).

Discussion

Oxidation State and Local Structure around Mn and Ni in $MnNiO_x$

The average oxidation state of Mn in $MnNiO_x$ under ORR conditions is higher than +3 and close to that in birnessite (~3.6). On the other hand, Ni exists as +2 with a small fraction of +3. This result is supported by XES as well as XANES. In addition, both Mn and Ni EXAFS point towards a layered structure for the ORR phase consisting of edge sharing M-O octahedra. While the first neighbor distances (Ni-O) are comparable to that in $Ni(OH)_2$, the second neighbor distance (Ni-O-M, where M could be Ni/Mn) is slightly shorter in the ORR phase (see ESI Table 1, 3.06 Å for Ni-Mn in $MnNiO_x$ vs 3.12 Å for Ni-Ni distances in $Ni(OH)_2$). This is likely due to the presence of a Ni(III) fraction in the Ni(II)
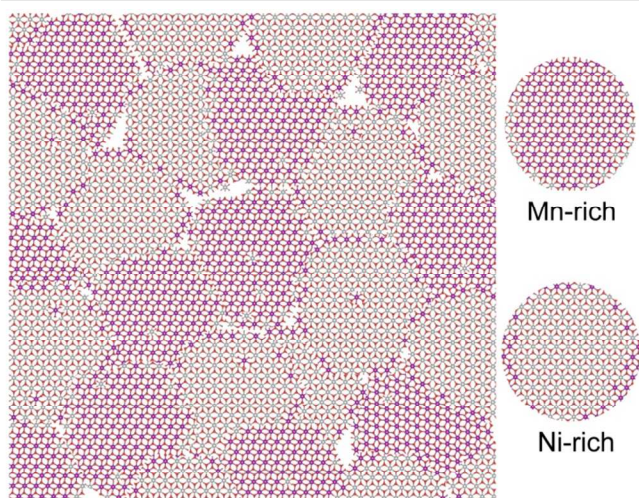
Fig. 7 Schematic representation of the suggested $MnNiO_x$ structure built from small domains representing Mn rich (purple) and Ni rich (grey) regions.

cluster. If Ni and Mn were mixed at the atomic level, we would expect Ni-metal distances from Ni EXAFS and Mn-metal distances from Mn EXAFS to be the same. A comparison of Ni and Mn EXAFS under ORR conditions (**Fig. S5a, Table S1**) clearly indicates that second neighbor distances are different in both cases. This shows that the MnO_x and NiO_x phases are not entirely mixed at the atomic scale, despite the fact that the electrochemical behavior of $MnNiO_x$ phase is different as compared to the pure oxide phases (Fig. 1b). In the XRD data of the dry as well as catalytically tested $MnNiO_x$ catalyst (**Fig. S5b**), long range order was not observed as the only visible diffraction peaks were either due to the blank Si_3N_4 window or the Au layer on the Si_3N_4. This suggests that the MnO_x and NiO_x domains are either amorphous or their cluster sizes are too small to be detectable in the XRD. The fact that the Mn and Ni EXAFS peak intensities highly resemble that of the bulk oxide samples, with visible peaks of the long-range interactions around 4 - 6 Å (ESI Fig. S2), shows that these domains are not amorphous, as that would have been accompanied by a reduced EXAFS peak intensity due to a highly disordered structure; thus it is expected that the material forms nano-domains too small for crystallinity to be observed by XRD.

Under OER conditions, Mn and Ni oxidation states were found to be ~ +4 and ~ +3.7 respectively. The EXAFS spectra of the OER catalyst show that the Ni local environment is similar to that of γ-NiOOH. The local structure of Mn in the OER phase shows some similarities with λ-MnO_2; however, there are some differences at longer distances where Mn and Ni EXAFS spectra are similar (**Fig. S5c**). Also, the Mn-metal and Ni-metal distances are nearly identical under OER conditions (ESI Table S1). However, this is not due to the mixing of Mn and Ni at the atomic level, but likely due to the structural similarity of the MnO_x and NiO_x phases during the OER. Reversible changes were observed in the EXAFS spectra between the ORR and OER phases, which underscores the importance of studying electrocatalytic materials under operating conditions, given the phase changes that materials can undergo. The detailed comparisons of the Mn and Ni EXAFS spectra of the $MnNiO_x$ catalyst with the Mn and Ni standards are shown in ESI Fig. S2, S4, and S5.
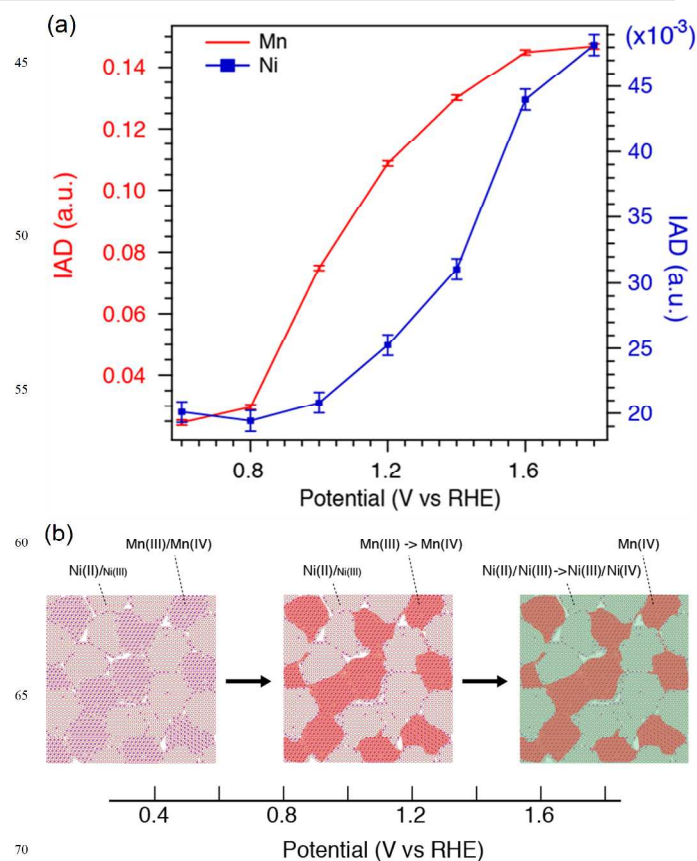

Fig. 8 (a) Absolute values of integrated spectral differences using the XES spectrum at 0.4 V as the reference. Calculation was done in the energy range 6471.0-6497.0 eV for Mn (red) and 8248.0-8276.0 eV for Ni (blue). **(b)** Schematic representation of sequential phase transitions upon changing potential.

Thus, the combined results of Mn and Ni EXAFS under ORR and OER conditions along with the XRD data provide us with a picture of mixed Mn- and Ni-rich nano-scale crystalline domains with their domain sizes below the XRD detection limit. A schematic representation of such a phase is shown in **Fig. 7.** The nano-scale texture, with Mn and Ni in close proximity at the active sites accessible by the electrolyte, may explain the observed differences in electrochemical behavior compared to the pure Mn and Ni oxide electrocatalysts (Fig. 1b).

The effect of Ni on the MnO_x bifunctional catalyst

Simultaneous detection of Mn and Ni XES signals using the wavelength-dispersive spectrometer provides us with information about how the MnO_x and NiO_x nano-phases respond and change their oxidation states during the step-wise electrochemical sweep, and how the redox change of each element is related to features in the cyclic voltammetry. The IAD values calculated for the spectral range of 6471.0-6497.0 eV for Mn and 8248.0-8276.0 eV for Ni are plotted in **Fig. 8a**, for the anodic potential sweep. The error bars correspond to the bandwidth of noise in the difference spectra (Fig. 5). The shift in the IAD value is related to a decrease in the energy difference between the $3p$ and $1s$ levels as well as the reduction in effective spin on the metal center with increasing oxidation state. For Mn, the IAD starts increasing after 0.8 V and the curve shows a fairly linear increase between 0.8-1.4 V, followed by a plateau at higher potentials. This is consistent with

the CV curve where there is no observable sharp peak that corresponds to Mn oxidation; however, by zooming-in (**Fig. S8**), a broad oxidation feature corresponding to Mn can be noticed at around 1.0 V. In the case of Ni, there is no considerable change in IAD values in the low potential range up to 1.0 V, after which the IAD value increases towards a plateau at high potentials. This is in accordance with the CV curve where a sharp oxidation peak appears between 1.2 and 1.4 V.

Comparable Mn oxidation states were observed between the pure MnO_x and $MnNiO_x$ electrocatalysts under ORR conditions. For the $MnNiO_x$, upon sweeping the potential from ORR to OER, the oxidation of Mn from Mn^{III} to Mn^{IV} advances at a lower potential followed by changes for Ni ($Ni^{II/III}$ to $Ni^{III/IV}$) at a higher potential. Such sequential phase transition can be pictorially viewed in **Fig. 8b**. The fact that the pure MnO_x electrocatalyst made under similar conditions did not show the same phase transition within the potential range of 0.7 V to 1.8 V (ESI **Fig S6b**) suggests that the presence of Ni plays an important role. We note that a potential of 1.9 V was required to observe a similar oxidation state (+4) in the pure MnO_x film (see ESI **Fig S6d**). At 1.8V, the current measured for the $MnNiO_x$ catalyst was twice as high as for the MnO_x catalyst. Also, the Mn oxidation state at this potential was measured to be higher for the $MnNiO_x$ film.

The electrocatalytic performance of this mixed $MnNiO_x$ film combines both the OER activity of NiO_x and the ORR activity of MnO_x, making it an efficient bifunctional catalyst. The association of nickel and manganese in a layered mixed oxide appears as a valid strategy to enhance the catalytic activities of both metals. In particular, the presence of Ni facilitates the access of manganese to higher oxidation states, which might improve the OER activity. Also, on the contrary to a pure MnO_x phase which was shown to convert from a spinel to a layered structure on going from ORR to OER,[25] the $MnNiO_x$ bifunctional catalyst studied here is active for the ORR and OER without any major structural change leading to improved reversibility. This implies less reorganization between ORR/OER cycles, which might have important implications on catalyst lifetime.

Conclusions

We have developed a method of detecting XES signals from multiple elements simultaneously by using a wavelength-dispersive multi-crystal spectrometer. This approach is suitable for studying various systems that contain multiple transition metal elements, and eliminates temporal and normalization errors that can arise from probing multiple elements separately. It is therefore ideal for following sequential chemistry at multiple sites accurately. In this particular study, we have elucidated key changes in structure and oxidation state for a $MnNiO_x$ bifunctional catalyst, examined under operating conditions for the oxygen reduction reaction and the oxygen evolution reaction. We have demonstrated the feasibility of the method proposed here, by applying it to study the effect of a secondary element, Ni, on the catalytic properties of the material. The presence of Ni was found to promote the access of Mn to higher oxidation state and shift the oxidation potential of Mn to a lower value. Under ORR conditions, an average oxidation state of +3.6 was observed for Mn whereas Ni mostly existed as Ni^{II}. In OER phase, Mn was found to exist as Mn^{IV} with Ni having an oxidation state close to

that in γ-NiOOH, i.e., +3.7.

The method described here can be applicable to time-resolved studies of natural and inorganic catalysts, electron transfer pigments, etc. at synchrotrons as well as X-ray free electron laser facilities, to follow the kinetics of catalytic reactions involving multi-metallic systems. While we focused on the $K\beta_{1,3}$ and $K\beta'$ transitions that are sensitive to the charge and spin density of metals, one can also probe other emission lines, in particular, the valence to core emission ($K\beta_{2,5}$ transitions). As these transitions are sensitive to the protonation state of metal ligands,[4] it will allow for the monitoring of movements of protons in inorganic and bioinorganic systems, where such a process is essential to understand catalytic mechanisms.

Experimental Section

Model Compounds

$NaNiO_2$ was synthesized by annealing Na_2O_2 and NiO in a stream of O_2 as reported previously.[32] $NaNiO_2$ was used to prepare γ-NiOOH by treating it with 5 mol equivalent of Br_2 in acetonitrile.[32] For β-NiOOH a suspension of $Ni(OH)_2$ in 3 M aqueous KOH was treated with 0.7 mol equivalents of Br_2. NiO, Na_2O_2, $Ni(OH)_2$, KOH, Br_2, and $K_2Ni(H_2IO_6)_2$ were purchased from Aldrich.

$Mn_3^{II,III,III}O_4$ was purchased from Sigma-Aldrich. The details of synthesis and characterization of β-$Mn^{IV}O_2$ and α-Mn_2O_3 are described in a previous study,[25] and the description of Mg^{2+} birnessite is reported in the work published by Webb *et. al.*[33] λ-MnO_2 was prepared according to the method reported by Hunter.[34] Briefly, appropriate amounts of Mn_2O_3 (99.99% Aldrich) and Li_2CO_3 ($\geq$99% Sigma-Aldrich) were mixed and heated in air at 850 °C for 1hr to prepare $LiMn_2O_4$. λ-MnO_2 was then obtained by treating $LiMn_2O_4$ with dilute HNO_3 (pH 1) for 45 minutes with constant stirring, and then drying the filtered solid at 90 °C in air.

Electrodeposition of Oxide Catalysts

$MnNiO_x$ was deposited onto a gold-coated silicon nitride (Au-Si_3N_4) membrane window via a sequential co-electrodeposition technique. Prior to electrodeposition, the as-received Si_3N_4 membrane window (1 μm thick membrane, part number NX10500F, Norcada) was sputter-coated with a 10 nm titanium layer followed by a 100 nm gold layer to establish electrical conductivity. The electrodeposition electrolyte was prepared by dissolving 0.551 g of manganous acetate (Aldrich, 99.99%), 0.560 g of nickel(II) acetate (Aldrich, 99.998%), and 0.639 g of sodium sulfate (Sigma-Aldrich, > 99.0%) in 45 mL of Millipore water. Electrodeposition was carried out in a N_2-purged three electrode electrochemical cell with the Au-Si_3N_4 membrane window as the working electrode, a graphite rod as the counter electrode, and an Ag|AgCl reference electrode. In a typical electrodeposition cycle, the potential was held at 0.57 V vs. Ag|AgCl to pass 2.5 mC of charge for Mn deposition before switching the potential to -0.88 V vs. Ag|AgCl to pass 2.5 mC of charge for Ni deposition. The system was then rested for 5 seconds before repeating the deposition again for a total of 20 cycles. The entire deposition process took roughly 5 minutes to complete. Separate NiO_x and MnO_x samples were also deposited onto Au-Si_3N_4 for comparison purposes. NiO_x on Au-Si_3N_4 was

synthesized by eliminating the manganous acetate from the deposition solution and also removing the potential hold at 0.57 V during electrodeposition, while MnO_x on $Au-Si_3N_4$ was synthesized by eliminating the nickel (II) acetate from the deposition solution and also removing the potential hold at -0.88 V during electrodeposition.

Physical Characterization

Scanning electron microscopy (SEM, FEI Magellan 400 XHR) was used to determine the thickness of $MnNiO_x$ on $Au-Si_3N_4$. Prior to SEM characterization, the membrane window was deliberately shattered and a shard of the $Au-Si_3N_4$ window was imaged. Shattering was necessary since the $Au-Si_3N_4$ window is surrounded by a supporting frame and electrodeposition typically results in more material deposition at the edges than in the middle. Imaging the unbroken membrane window would have resulted in an overestimation of the actual catalyst thickness on the $Au-Si_3N_4$ window. The sample stage was tilted at a 60 degree angle and a 15 pA beam current of 1 kV and a backscatter electron detector were used. The crystallinity of the samples was examined using X-ray diffraction (XRD, Phillips PANalytical X'Pert Pro) with Cu Kα radiation (λ = 1.542 Å) operated at 45 kV and 40 mA. The scan range was between 10 and 90 degrees, while the degrees per step and time per step were 0.02 degrees and 0.5 seconds respectively.

Electrochemical Characterization

The oxygen reduction and oxygen evolution activities of the $MnNiO_x$, MnO_x, and NiO_x catalysts were first evaluated in a three electrode electrochemical cell with a graphite rod counter electrode, an Ag|AgCl reference electrode, and 0.1 M potassium hydroxide (KOH) electrolyte. The headspace of the cell was purged with O_2. Cyclic voltammetry (CV) was carried out at a sweep rate of 20 mV/s in a potential region of 0.35 V to 1.78 V vs. reversible hydrogen electrode (RHE). All scans were 100 % IR-compensated. The potential scale was calibrated to RHE using a platinum wire as the working electrode in a hydrogen-saturated electrolyte. The reversible hydrogen potential (0.00 V versus RHE) was taken to be the potential at which the current is zero, and a value of -0.957 V was obtained.

In situ XES data collection

XES data collection was performed at beamline 5.0.2 of the Advance Light Source (ALS). The incident X-ray beam, focused to 1 x 2 mm^2 (vertical x horizontal), had a flux of ~ 4x10^{12} photons/sec at an energy of 10.4 keV. XES spectra were recorded on two Pilatus100k PSD detectors (Dectris) by means of a multi-crystal wavelength-dispersive hard X-ray spectrometer based on the von Hamos geometry. The emission energy was calibrated to the published value of 6490.4 eV (the 1st moment from the 6485 – 6495 eV region) of Mn_2O_3 for Mn.[35] For Ni XES, the 1st moment energy of $Ni(OH)_2$ was defined as 8263.7 eV, calculated from the 8248.0-8276.0 eV region. All data were collected at room temperature with an acquisition time of 60 minutes for each spectrum.

XAS Data Collection

The XAS measurements at Mn and Ni *K*-edges were performed on beamline 7-3 at Stanford Synchrotron Radiation Laboratory (SSRL) with an average current of 500 mA at an electron energy of 3.0 GeV. A Si (220) double crystal was used to monochromatize the radiation and detune the radiation to 50% of flux maximum at Mn/Ni *K*-edge, thereby attenuating the effects of higher harmonics. Fluctuations in the incident beam intensity were monitored using a N_2-filled chamber (I_0) in front of the sample. XAS spectra were also collected for the reference samples mentioned for XES and energy was calibrated using a Ni foil or $KMnO_4$ placed between two N_2-filled chambers (I_1 and I_2) after the sample. In case of Ni, the spectra were calibrated with respect to the first peak maximum of the first derivative for Ni foil (8333.0 eV) whereas the intense pre-edge peak for the Mn *K*-edge of $KMnO_4$ was calibrated to 6543.3 eV. For *in situ* measurements, the energy was calibrated using a monochrometer glitch in the I_0 reading. The data was collected at room temperature in fluorescence excitation mode using a 30 element Ge detector (Canberra).

Data analysis was done using the standard programs based on IFEFFIT.[36, 37] The spectra were normalized with respect to the edge height after subtracting the pre-edge and post-edge backgrounds using Athena software. To extract EXAFS oscillations, background was removed in *k*-space using a five-domain cubic spline. The resulting k-space data, $k^3\chi(k)$, was then Fourier transformed.

For comparison, XAS and XES spectra of several Mn oxide powder samples, $Mn^{II}O$, $Mn^{III}_2O_3$, $Mn^{IV}O_2$, $Mn^{III}OOH$, and Mn minerals like birnessite (Mn^{III}/Mn^{IV}) and todorokite (Mn^{III}/Mn^{IV}) were collected. For Ni reference samples, the XES spectra of $Ni^{II}(OH)_2$, β–$Ni^{III}OOH$, γ–$NiOOH$, $NaNi^{III}O_2$, and $K_2Ni^{IV}(H_2IO_6)_2$ (potassium nickel(IV) paraperiodate, NiPPI) were collected. The XAS samples of these model compounds were prepared by diluting them with boron nitride (1% w/w) and enclosing the powder in an aluminum holder with Kapton tape windows on both sides. For XES, the compounds were used without dilution.

Electrochemical Cell Setup for *In Situ* Studies

An H-shaped electrochemical cell was used for *in situ* X-ray spectroscopy, in which the Si_3N_4 window was mounted on one surface. The electrochemical cell was positioned at an angle of 45° between the surface of the sample and the incident X-ray beam. In the setup, the backside of Si_3N_4 window was exposed to X-rays, while the front side of the Si_3N_4 window with electrodeposited MnO_x on Au/Ti layer faced into the interior of the two-compartment electrochemical cell. Electrochemistry was performed in ambient air using an Ag|AgCl reference electrode, a platinum wire counter electrode, and 0.1 M KOH electrolyte. Although the RHE calibration was not performed during *in-situ* XES/XAS characterization, we utilized the same shift of 0.957 V for the Ag|AgCl reference electrode as measured in the laboratory to report potentials vs. RHE. After preparing the electrochemical cell for *in-situ* XES/XAS measurements, the resistance between the working and reference electrodes was measured to ensure proper electrical contact between the potentiostat and catalyst on $Au-Si_3N_4$.

Notes and references

aPhysical Biosciences Division, Lawrence Berkeley National Laboratory, Berkeley, CA 94720, USA.
40 *bDepartment of Chemical Engineering, Stanford University, Stanford, CA 94305, USA.*
cSLAC National Accelerator Laboratory, 2575 Sand Hill Rd., Menlo Park, CA 94025, USA.
dJoint Center for Artificial Photosynthesis, Lawrence Berkeley National
45 *Laboratory, Berkeley, CA 94720, USA.*
eAdvanced Light Source, Lawrence Berkeley National Laboratory, Berkeley, CA 94720, USA
fDepartment of Chemistry, University of California at Santa Cruz, Santa Cruz, CA 95060, USA.
50 *#Present Address: Synchrotron SOLEIL, L'Orme des Merisiers, Saint-Aubin, 91191 Gif-sur-Yvette, France.*
%Present Address: Technical University of Munich, Lichtenbergstrasse 4, 85748 Garching, Germany.
*Corresponding authors: jaramillo@stanford.edu, jyano@lbl.gov
55 **Author Contributions:** T.F.J. and J.Y. conceived experiment; S.G., J.W.D.N., R.A-M., J.K., U.B., V.K.Y., T.F.J. and J.Y. designed experiment;S.G., J.W.D., and Y.G. prepared samples; R.A-M., J.K., D.S., T-C. W. and P.Z. set up the XES instrument; S.G., B.L-K., and Y.G. run the XAS experiment; S.G., J.W.D.N., R.A-M., J.K., D.S., E.A., B.L-K.,
60 Y.G., T-C. W. and J.Y. performed the XES experiment; S.G., J.W.D.N.,

1. P. Glatzel and U. Bergmann, *Coordination Chemistry Reviews*, 2005,
70 **249**, 65-95.
2. K. M. Lancaster, M. Roemelt, P. Ettenhuber, Y. Hu, M. W. Ribbe, F. Neese, U. Bergmann and S. DeBeer, *Science*, 2011, **334**, 974-977.
3. Y. Pushkar, X. Long, P. Glatzel, G. W. Brudvig, G. C. Dismukes, T. J. Collins, V. K. Yachandra, J. Yano and U. Bergmann, *Angewandte*
75 *Chemie International Edition*, 2010, **49**, 800-803.
4. B. Lassalle-Kaiser, T. T. Boron III, V. Krewald, J. Kern, M. A. Beckwith, M. U. Delgado-Jaime, H. Schroeder, R. Alonso-Mori, D. Nordlund and T.-C. Weng, *Inorganic chemistry*, 2013, **52**, 12915-12922.
80 5. H. Kropp, A. E. King, M. M. Khusniyarov, F. W. Heinemann, K. M. Lancaster, S. DeBeer, E. Bill and K. Meyer, *Journal of the American Chemical Society*, 2012, **134**, 15538-15544.
6. C. J. Pollock, M. U. Delgado-Jaime, M. Atanasov, F. Neese and S. DeBeer, *Journal of the American Chemical Society*, 2014, **136**, 9453-
85 9463.
7. R. Alonso-Mori, J. Kern, D. Sokaras, T.-C. Weng, D. Nordlund, R. Tran, P. Montanez, J. Delor, V. K. Yachandra and J. Yano, *Review of Scientific Instruments*, 2012, **83**, 073114.
8. J. Kern, R. Alonso-Mori, J. Hellmich, R. Tran, J. Hattne, H.
90 Laksmono, C. Glöckner, N. Echols, R. G. Sierra and J. Sellberg, *Proceedings of the National Academy of Sciences*, 2012, **109**, 9721-9726.
9. J. Kern, R. Alonso-Mori, R. Tran, J. Hattne, R. J. Gildea, N. Echols, C. Glöckner, J. Hellmich, H. Laksmono, R. G. Sierra, B. Lassalle-
95 Kaiser, S. Koroidov, A. Lampe, G. Han, S. Gul, D. DiFiore, D. Milathianaki, A. R. Fry, A. Miahnahri, D. W. Schafer, M. Messerschmidt, M. M. Seibert, J. E. Koglin, D. Sokaras, T.-C. Weng, J. Sellberg, M. J. Latimer, R. W. Grosse-Kunstleve, P. H. Zwart, W. E. White, P. Glatzel, P. D. Adams, M. J. Bogan, G. J. Williams, S.
100 Boutet, J. Messinger, A. Zouni, N. K. Sauter, V. K. Yachandra, U. Bergmann and J. Yano, *Science*, 2013, **340**, 491-495.
10. J. Kern, R. Tran, R. Alonso-Mori, S. Koroidov, N. Echols, J. Hattne, M. Ibrahim, S. Gul, H. Laksmono and R. G. Sierra, *Nature communications*, 2014, **5**.
105 11. R. Alonso-Mori, J. Kern, R. J. Gildea, D. Sokaras, T.-C. Weng, B. Lassalle-Kaiser, R. Tran, J. Hattne, H. Laksmono and J. Hellmich, *Proceedings of the National Academy of Sciences*, 2012, **109**, 19103-19107.
12. M. W. Louie and A. T. Bell, *Journal of the American Chemical*
110 *Society*, 2013, **135**, 12329-12337.
13. A. C. Garcia, A. D. Herrera, E. A. Ticianelli, M. Chatenet and C. Poinsignon, *Journal of The Electrochemical Society*, 2011, **158**, B290-B296.
14. Q. Wu, L. Jiang, L. Qi, E. Wang and G. Sun, *International Journal of*
115 *Hydrogen Energy*, 2014, **39**, 3423-3432.
15. P. Quaino, N. Luque, R. Nazmutdinov, E. Santos and W. Schmickler, *Angewandte Chemie International Edition*, 2012, **51**, 12997-13000.
16. J. W. D. Ng, Y. Gorlin, D. Nordlund and T. F. Jaramillo, *Journal of The Electrochemical Society*, 2014, **161**, D3105-D3112.
120 17. J. W. D. Ng, M. Tang and T. F. Jaramillo, *Energy & Environmental Science*, 2014, **7**, 2017-2024.
18. P. Oliva, J. Leonardi, J. Laurent, C. Delmas, J. Braconnier, M. Figlarz, F. Fievet and A. d. Guibert, *Journal of Power sources*, 1982, **8**, 229-255.
125 19. D. A. Corrigan and S. L. Knight, *Journal of The Electrochemical Society*, 1989, **136**, 613-619.
20. J. Desilvestro, D. A. Corrigan and M. J. Weaver, *Journal of The Electrochemical Society*, 1988, **135**, 885-892.
21. G. Peng, F. M. F. deGroot, K. Haemaelaeinen, J. A. Moore, X.
130 Wang, M. M. Grush, J. B. Hastings, D. P. Siddons and W. H.

Armstrong, *Journal of the American Chemical Society*, 1994, **116**, 2914-2920.

22. P. Glatzel, U. Bergmann, F. M. F. de Groot and S. P. Cramer, *Physical Review B*, 2001, **64**, 045109.

23. G. Vankó, T. Neisius, G. Molnár, F. Renz, S. Kárpáti, A. Shukla and F. M. F. de Groot, *The Journal of Physical Chemistry B*, 2006, **110**, 11647-11653.

24. G. Vankó, J.-P. Rueff, A. Mattila, Z. Németh and A. Shukla, *Physical Review B*, 2006, **73**, 024424.

25. Y. Gorlin, B. Lassalle-Kaiser, J. D. Benck, S. Gul, S. M. Webb, V. K. Yachandra, J. Yano and T. F. Jaramillo, *Journal of the American Chemical Society*, 2013, **135**, 8525-8534.

26. J. E. Post and D. R. Veblen, *American Mineralogist*, 1990, **75**, 477-489.

27. S. Ching, D. J. Petrovay, M. L. Jorgensen and S. L. Suib, *Inorganic Chemistry*, 1997, **36**, 883-890.

28. D. Golden, C. Chen and J. Dixon, *Clays and Clay Minerals*, 1987, **35**, 271-280.

29. D. P. Dubal, A. D. Jagadale and C. D. Lokhande, *Electrochimica Acta*, 2012, **80**, 160-170.

30. Y. Dai, K. Wang and J. Xie, *Applied Physics Letters*, 2007, **90**, -.

31. Y. F. Shen, R. P. Zerger, R. N. DeGuzman, S. L. Suib, L. McCurdy, D. I. Potter and C. L. O'Young, *Science*, 1993, **260**, 511-515.

32. X. Yang, K. Takada, M. Itose, Y. Ebina, R. Ma, K. Fukuda and T. Sasaki, *Chemistry of Materials*, 2007, **20**, 479-485.

33. S. Webb, B. Tebo and J. Bargar, *American Mineralogist*, 2005, **90**, 1342-1357.

34. J. C. Hunter, *Journal of Solid State Chemistry*, 1981, **39**, 142-147.

35. U. Bergmann, J. Bendix, P. Glatzel, H. B. Gray and S. Cramer, *Journal of Chemical Physics*, 2002, **116**, 2011-2015.

36. M. Newville, *Journal of synchrotron radiation*, 2001, **8**, 322-324.

37. B. Ravel and M. Newville, *Journal of synchrotron radiation*, 2005, **12**, 537-541.